Qi, Qi, Hossain, Md. Moinul, Lu, Gang, Xu, Chuanlong and Huang, Yizhi (2026) ***Refocusing performance of multi-spectral light field camera through spectrally and depth-resolved flame imaging.*** **Optics & Laser Technology, 200 . ISSN 0030-3992.**

The version of record is available from
https://doi.org/10.1016/j.optlastec.2026.115127

This document version
Author's Accepted Manuscript

DOI for this version

Refocusing Performance of Multi-Spectral Light Field Camera through Spectrally and Depth-Resolved Flame Imaging

1. **Qi Qi**
School of Engineering, Mathematics and Physics, University of Kent, Canterbury, Kent, CT2 7NT, UK
q.qi@kent.ac.uk

2. **Md. Moinul Hossain * (corresponding author)**
School of Engineering, Mathematics and Physics, University of Kent, Canterbury, Kent, CT2 7NT, UK
m.hossain@kent.ac.uk

3. **Gang Lu**
School of Engineering, Mathematics and Physics, University of Kent, Canterbury, Kent, CT2 7NT, UK
g.lu@kent.ac.uk

4. **Chuanlong Xu**
National Engineering Research Center of Power Generation Control and Safety, School of Energy and Environment, Southeast University, Nanjing 210096, China
chuanlongxu@seu.edu.cn

5. **Yizhi Huang**
National Engineering Research Center of Power Generation Control and Safety, School of Energy and Environment, Southeast University, Nanjing 210096, China
230189043@seu.edu.cn

Refocusing Performance of Multi-Spectral Light Field Camera through Spectrally and Depth-Resolved Flame Imaging

Qi Qi, Md. Moinul Hossain*, Gang Lu, Chuanlong Xu, Yizhi Huang

Abstract

Flames are highly dynamic, and their radiation, temperature, and radical emissions vary with combustion conditions. Different spectral bands reveal distinct radical emissions. Flames are also inherently three-dimensional (3D), and imaging at multiple depths is needed to resolve spatial variations. Multi-spectral imaging enables the capture of 3D flame characteristics through refocused imaging across spectra and depths, simultaneously capturing spatial, angular, and spectral data. This study presents a systematic investigation of how various filter array designs and multi-spectral light field camera (MS-LFC) configurations influence the quality of refocused flame images. Simulations were conducted to assess the effects of filter array designs and MS-LFC configurations on the sharpness and structural similarity of refocused images. The results show that centrally distributed spectral filters and a sufficiently dense set of sub-aperture images significantly enhance the sharpness and structural similarity of refocused flame images, enabling accurate depth-resolved flame reconstruction across different spectra. Conversely, reduced angular sampling leads to sparser data acquisition, degrading image similarity and overall quality, except at the focal plane, where refocusing is less affected. A detailed analysis of these findings offers valuable guidance for the design and optimization of MS-LFC systems, contributing to improved accuracy and efficiency in spectrally and depth-resolved flame imaging for combustion diagnostics.

1. Introduction

Flames exhibit highly dynamic and complex behaviours, with their radiation intensity, temperature and radical emission distributions varying significantly under different combustion conditions [1, 2]. Depending on the specific combustion reactions involved, flames emit light across a wide spectral range from ultraviolet to infrared [3, 4]. Since each spectral band corresponds to emissions from distinct chemical species and temperature ranges, multi-spectral flame imaging offers valuable insights into combustion characteristics [5, 6]. Moreover, the three-dimensional (3D) structure of a flame often shows depth-dependent variations in temperature and species concentration. Consequently, accurate imaging across multiple spectra and is crucial for comprehensive combustion diagnostics, fire safety engineering, and industrial process monitoring [7].

Light field cameras (LFCs) are increasingly being used in combustion studies due to their ability to capture four-dimensional (4D) light field information in a single exposure. This is achieved by utilising a microlens array (MLA) positioned between the main lens and the sensor to record both spatial and angular data [8, 9]. The recorded LF enables digital refocusing by computationally integrating the angular samples to synthesize images focused at different depths [10]. Therefore, unlike conventional cameras, where the focus is fixed at the time of capture, LFCs allow for post-capture refocusing, providing flexible depth selection without mechanical adjustment. This capability preserves depth-dependent features and enhances the analysis of complex 3D objects such as flames [11]. For instance, Zhao et al. [12] proposed an optical sectioning tomographic technique for 3D flame temperature measurement based on LF imaging. Both simulation and experimental results showed that the LFC can reconstruct the original radiative intensity distribution of each sectional layer of the flame. Liu et al. [13] enhanced the LF sectioning pyrometry and provided a quantitative analysis of its spatial resolution for measuring flame temperatures. Zhang et al. [14] developed a 3D flame temperature reconstruction method using a LFC. The digital refocusing technique was used to obtain several 2D image sequences at different depths. However, these techniques are limited to single-wavelength measurements or rely on Bayer filter arrays for color imaging. Flames emit radiation across multiple spectral bands, each carrying distinct physical and chemical information, which has not been investigated. Single-wavelength imaging fails to capture the multi-spectral features of combustion, while Bayer-filter-based systems suffer from low spectral resolution and crosstalk between color channels [15]. As a result, conventional LFCs provide limited multi-dimensional spectral information, restricting the ability to capture flame parameters accurately, such as temperature distribution and species concentration.

To address these challenges, a multi-spectral LF imaging technique was developed to overcome the limitations of conventional LF imaging. This technique allows for the simultaneous collection of spatial, angular and spectral information. For example, Levoy [16] proposed a multi-spectral light field camera (MS-LFC) that incorporates a filter array at the main lens, which was later implemented by Horstmeyer et al.[17]. In this design, the MLA is positioned one focal length away from the sensor, and each microlens forms a micro-image of the filter array. This configuration enables the simultaneous capture of 27 spectral channels covering the 400 nm - 700 nm range. The compatibility of this MS-LFC with a variety of main lenses and focal length adjustment. Fahringer et al. [18] developed a MS-LFC equipped with a filter containing seven discrete wavelength bands, enabling the simultaneous imaging of multiple spectra, and also proposed a method for artifact mitigation and correction. Huang et al. [19] developed a cage-typed MS-LFC incorporating a visible filter array, allowing for high-resolution spectral information acquisition. A joint decoding method is proposed, which integrates aberration correction to improve spatial data quality. The unfocused MS-LFC has also been implemented in flame/surface parameter measurements [20]. It demonstrates that by decoupling a raw multi-spectral LF image and utilizing traditional multi-wavelength pyrometry algorithms, the accurate scalar field of surface temperature distribution can be reconstructed. Kelly et al. [21] presented a 2D high-temperature pyrometer based on a MS-LFC integrated with a continuous wavelength filter. Experiments showed that the pyrometer is capable of simultaneously measuring the temperatures of copper in both liquid and solid phases, achieving a temperature accuracy better than 5%. Subsequently, the extended MS-LFC is used to realize simultaneous measurements of velocity fields, temperature distributions, and CH* distributions [22]. Although the aforementioned studies demonstrate the potential of the MS-LFC for multi-dimensional combustion parameter measurement, several limitations remain to be resolved. For examples,

- Existing studies primarily focus on 2D distribution measurement and do not fully utilise the depth-resolving capabilities of LF imaging.
- Although various filter arrays have been introduced to realise multi-spectral acquisition, the trade-offs among angular, spatial and spectral resolution have not been thoroughly analysed and the impact of filter array design on depth estimation accuracy remains poorly understood.
- There is a lack of systematic evaluation of refocused flame image quality across different depths and spectra using MS-LFC, which makes it difficult to fully assess its performance in depth-resolved multispectral imaging.

Addressing these issues will be crucial for establishing the MS-LFC as a reliable and robust tool for simultaneous 3D flame parameter measurements in combustion studies. Therefore, this study presents a systematic investigation of the quality of refocused flame images captured under different filter array designs and MS-LFC configurations. Image quality was evaluated across multiple depths to investigate the limitations of existing studies, mainly focusing on 2D distributions, allowing a more comprehensive characterization of the flame's 3D structure. The effects of different spectral filter arrangements on angular, spatial, and spectral resolution, as well as on image sharpness and similarity, were analyzed to clarify the trade-offs inherent in multi-spectral LF imaging. Sharpness and similarity metrics were employed to quantify the influence of MS-LFC configurations and filter array designs on refocused image quality across different spectra and depths, providing a detailed assessment of the refocusing performance of the MS-LFC. The results offer practical guidelines for optimizing MS-LFC systems, enhancing their capability for accurate, depth-resolved, multispectral flame imaging, and contributing to improved combustion diagnostics, fire safety evaluation, and industrial process monitoring.

2. Methodology

Figure 1 illustrates the proposed strategy for refocused flame image reconstruction at different depths under varying spectra using a MS-LFC. The process commences with configuring the MS-LFC and flame parameters, followed by the simulation of the raw multi-spectral LF flame image. The subsequent step involves decoding the raw LF data to generate sub-aperture images from different angular perspectives. Finally, a LF refocusing algorithm is applied to reconstruct depth-resolved flame images under different spectra.

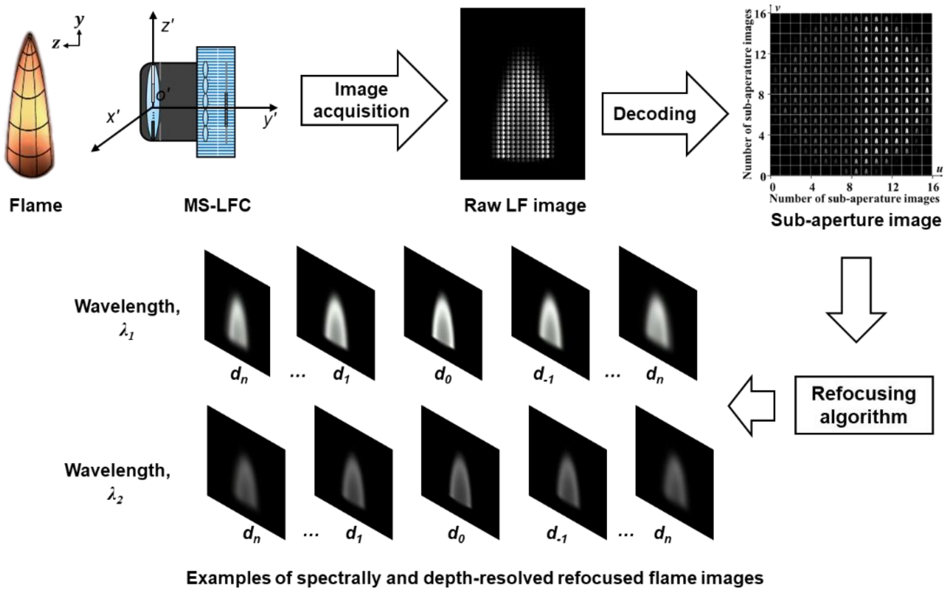

Fig. 1. The proposed strategy for refocused flame image reconstruction at different depths under different spectra.

2.1 Principle of the MS-LFC

The MS-LFC is conceptually derived from the conventional LFC, which employs a microlens array (MLA) positioned in front of the photosensor to capture the spatial and angular information of incident light simultaneously. In the LFC, rays from a single point on the flame converge at a single point on the image plane of the main lens. The MLA then separates these rays according to their directions, forming focused images on the pixel arrays beneath each microlens. Each of these pixel arrays is referred to as a sub-image or a macropixel [8]. To extend this concept to a MS-LFC system, a spectral discriminator is incorporated into the optical system. In this study, a filter array is inserted at the aperture of the main lens. Schematic illustrations of both the conventional LFC and MS-LFC are presented in Fig. 2. As the ray passes through the main lens in the MS-LFC, it is further encoded spectrally, such that each pixel is associated with a specific wavelength band. It is noted that various configurations can be employed in the design and arrangement of the filter array based on applications. Such flexibility enables more precise control over the central wavelength and bandwidth of each filter, which is advantageous for isolating specific spectral features of interest. Different configurations of the filter array can therefore be adopted to meet various application requirements. The spectral resolution ranges from a minimum, when the system measures only a single wavelength, to a maximum, when each pixel beneath a microlens is uniquely assigned to a distinct wavelength. This flexibility enables precise control over the central wavelength and bandwidth of each filter, which is advantageous for isolating specific spectral features of interest.

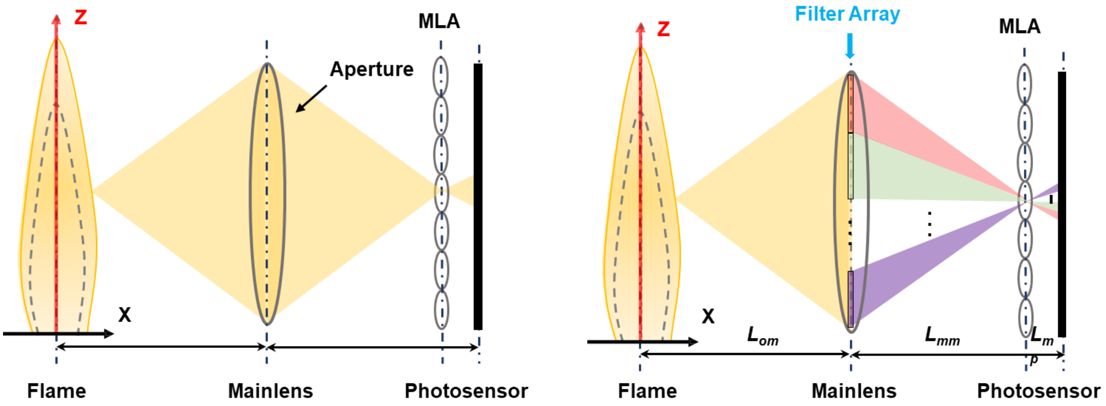

(a) LFC

(b) MS-LFC

Fig. 2. Schematic illustrations of the LFC and MS-LFC configuration.

A conventional method to characterize the LF is the two-plane parameterization, in which each ray is parameterized by its intersection points on two parallel planes separated by a known distance [23]. Assuming that the lens plane and the sensor plane are infinite, and considering the rays that travel between them, the 4D LF can be described as shown in Fig. 3. The distance between the lens plane and the sensor plane is denoted as F, and $L_F(u, v, x, y)$ represents the radiance of the ray that passes through the lens plane at (u, v) and strikes the sensor plane at (x, y). Therefore, $E_F(x, y)$, the LF image on the photosensor can be expressed as,

$$E_F(x,y) = \iint L_F(u,v,x,y)dudv \tag{1}$$

For the MS-LFC, as the light is imaged through the main lens, the wavelength of each ray is encoded into the recorded LF $L_F(u, v, x, y, \lambda)$, thereby associating each pixel with a specific wavelength band.

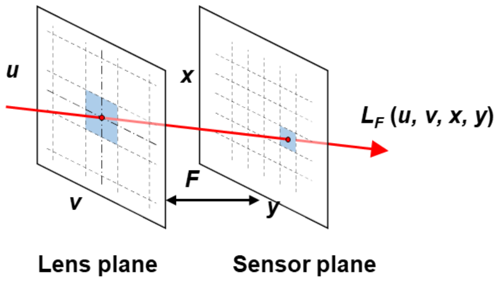

Fig. 3. Parameterization of the 4D LF illustrated by lens and sensor planes.

2.2 Light Field Refocusing Technique

LF refocusing utilizes 4D LF information to computationally generate images focused on different depths by integrating angular ray information from multiple viewpoints, thereby enabling post-capture focal adjustment and depth analysis. The resulting images are referred to as refocused images. Fig. 4 shows a diagram that illustrates how a ray is parametrized by the lens, sensor and refocused planes. During refocusing, the LF information can be used to generate a refocused image at any depth F'. By similar triangles, the ray that intersects the lens plane at u and the refocused plane at x', also intersects the sensor plane x at $(x'-u)\ F/F'$. Although the diagram only shows the 2D case involving x and u, the same relationship holds for the y and v dimensions. If $F' = \alpha F$, where α defines the relative depth, the $L_{\alpha F}(u, v, x, y)$ can then be written as,

$$L_{\alpha F}(u,v,x',y') = L_F\left(u,v,u+\frac{(x'-u)}{\alpha},v+\frac{(y'-v)}{\alpha}\right) \tag{2}$$

Therefore, $E_{\alpha F}(x',y')$, the LF image on the photosensor corresponding to depth F' is expressed as follows,

$$E_{\alpha F}(x',y') = \iint L_F\left(u,v,u+\frac{(x'-u)}{\alpha},v+\frac{(y'-v)}{\alpha}\right)dudv \tag{3}$$

Based on the above equations, the refocused images under different depths F' can be calculated by changing the relative depth α.

For the MS-LFC, the same refocusing method is adopted. Specifically, each spectral band captures a distinct 4D spectral LF data, and the refocusing technique can be independently applied to each spectrum. This allows for the reconstruction of refocused images at various depths under each spectrum. By combining the refocused images across all spectrum bands, the MS-LFC can provide information with both depth and spectral resolution.

In this study, the LF refocusing algorithm used is based on frequency domain processing. The spatial-angular LF data is transformed into the frequency domain using the Fourier transform, where shifts corresponding to different focal planes become phase modulations. By applying depth-dependent phase shifts to the frequency spectra of each angular view, the algorithm generates refocused images at desired refocused planes. An inverse Fourier transform is then performed to obtain the final refocused image. This approach allows efficient and accurate digital refocusing [13, 24] of the flames.

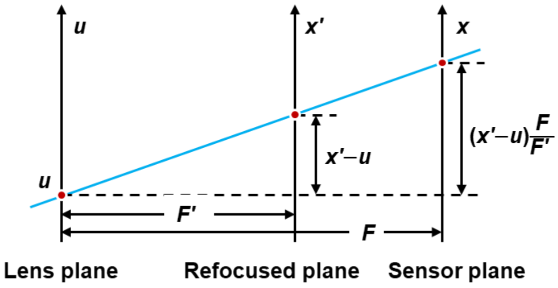

Fig. 4. Principle of the LF refocusing technique.

2.3 Quality Assessment

To evaluate the quality of the refocused images produced by both the LFC and MS-LFC, two metrics are employed: sharpness and similarity. The sharpness metric is used to assess the visual clarity of the refocused images at each depth, indicating how well the image is brought into focus. The similarity metric evaluates the consistency between refocused images, reflecting the degree of alignment and structural preservation.

A. Sharpness Assessment

For the sharpness metric, the Tenengrad function is adopted, which is a no-reference image quality assessment method. Due to its robustness to noise and computational efficiency, this method is well-suited for assessing the sharpness of refocused images in LF imaging [19]. It quantifies sharpness by computing the gradient magnitude of the image using the Sobel operator, thereby emphasizing edge strength and spatial details [25]. Given a grayscale refocused image, $I(x, y)$, the image gradients in the horizontal and vertical directions are computed as,

$$G_x(x,y) = (I * S_x)(x,y), \qquad G_y(x,y) = \left(I * S_y\right)(x,y) \tag{4}$$

where G_x and G_y are the gradients along the horizontal and vertical direction, respectively. S_x and S_y are the corresponding Sobel kernels. The symbol $*$ denotes the convolution operation.

The gradient magnitude at each pixel is then computed as,

$$G(x,y) = \sqrt{G_x(x,y)^2 + G_y(x,y)^2} \tag{5}$$

The Tenengrad sharpness value T is obtained by summing the squared gradient magnitudes across the entire image, with a threshold τ applied to suppress noise,

$$T = \sum_{x,y} G(x,y)^2 \cdot \mathbf{1}_{\{G(x,y)>\tau\}} \tag{6}$$

where, $\mathbf{1}_{\{G(x,y)>\tau\}}$ is the indicator function that equals 1 when the condition is satisfied and 0 otherwise.

B. Similarity Assessment

To quantitatively assess the structural fidelity of the refocused images, the Structural Similarity Index Measure (SSIM) is employed. The SSIM is an image quality assessment metric that evaluates the similarity between two images I_r and I_t, in terms of luminance, contrast, and structural information [26]. The SSIM index is computed as:

$$\mathrm{SSIM}(I_r, I_t) = [l(I_r, I_t)]^{\alpha} \cdot [c(I_r, I_t)]^{\beta} \cdot [s(I_r, I_t)]^{\gamma} \tag{7}$$

where

$$\begin{cases} l(I_r, I_t) = \frac{2\mu_r\mu_t + C_1}{\mu_r^2 + \mu_t^2 + C_1} \\ c(I_r, I_t) = \frac{2\sigma_r\sigma_t + C_2}{\sigma_r^2 + \sigma_t^2 + C_2} \\ s(I_r, I_t) = \frac{\sigma_{rt} + C_3}{\sigma_r\sigma_t + C_3} \end{cases} \tag{8}$$

where, $l(\cdot)$, $c(\cdot)$, and $s(\cdot)$ represent the luminance, contrast and structure comparison function. α, β and γ are their respective weights. μ_r and μ_t are the mean intensities of I_r and I_t, σ_r and σ_t are their standard deviations, and σ_{rt} is the covariance between the two patches. The positive constants C_1, C_2, and C_3 are used to avoid a null denominator, with $C_3 = C_2/2$ commonly used. When $\alpha = \beta = \gamma = 1$, the SSIM formula can be simplified to:

$$\mathrm{SSIM}(I_r, I_t) = \frac{(2\mu_r\mu_t + C_1)(2\sigma_{rt} + C_2)}{(\mu_r^2 + \mu_t^2 + C_1)(\sigma_r^2 + \sigma_t^2 + C_2)} \tag{9}$$

The SSIM values range from 0 to 1, where values closer to 1 indicate greater structural similarity.

3. Results and Discussions

3.1 Simulation Setup

Numerical simulations are conducted to evaluate the quality of refocused flame images obtained by the MS-LFC under various filter array designs and camera configurations. In this study, a cylindrical simulated flame with a unimodal temperature distribution is considered. Detailed descriptions of the flame model can be found elsewhere in [27]. The parameters of the MS-LFC used in the simulation are listed in Table 1. Two MS-LFC configurations based on the number of pixels and sizes are considered to investigate their impact on refocusing performance. For example, in configuration 1, the pixel size is

3 μm×3 μm, resulting in 32 pixels across the diameter of each sub-image, and in configuration 2, the pixel size is 6 μm×6 μm, giving 16 pixels across the diameter of each sub-image [28, 29].

For the MS-LFC, four different filter array designs are also proposed to explore the trade-offs between spectral resolution and refocusing performance, as shown in Fig. 5. These designs employ four representative visible wavelengths: $\lambda1$ = 610 nm, $\lambda2$ = 540 nm, $\lambda3$ = 515 nm and $\lambda4$ = 460 nm. These provide effective spectral sampling of flame radiation while remaining compatible with the MS-LFC system design. The selected wavelengths span the visible spectrum from blue to red, enabling the capture of key spectral variations in flame emission. In particular, the wavelengths at 460 nm and 515 nm correspond to prominent emission features of excited radicals such as CH* and C_2*, making them sensitive to high-temperature and chemically active regions. The wavelength at 540 nm is close to the peak spectral sensitivity of typical Charge-Coupled Device (CCD) and Complementary Metal–Oxide–Semiconductor (CMOS) sensors, ensuring high signal-to-noise imaging. The wavelength at 610 nm is mainly dominated by soot-related broadband radiation characteristic of relatively lower-temperature or soot-rich flame regions. These designs are based on four common visible wavelengths, which are λ_1 = 610 nm, λ_2 = 540 nm, λ_3 = 515 nm and λ_4 = 460 nm. Case 1 employs a single wavelength (i.e., λ_2 = 540 nm), enabling the evaluation of refocusing performance with full angular sampling. Case 2 incorporates two wavelengths (i.e., λ_1 = 610 nm and λ_2 = 540 nm), introducing spectral diversity while maintaining a reasonable level of angular resolution. Case 3 utilizes three wavelengths (i.e., λ_1 = 610 nm, λ_2 = 540 nm, and λ_4 = 460 nm) to further enhance spectral variation. Case 4 uses four wavelengths (i.e., λ_1 = 610 nm, λ_2 = 540 nm, λ_3 = 515 nm, and λ_4 = 460 nm) to explore a higher degree of spectral diversity, with a corresponding trade-off in angular sampling. The MATLAB platform with custom code is used to perform the LF refocusing calculations.

Table 1. The parameters of the MS-LFC.

Symbol	**Description**	**Value**	
		Configuration 1	**Configuration 2**
d_p	Pixel size	**3 μm×3 μm**	**6 μm×6 μm**
N_p	Number of pixels on the diameter of each sub-image	**32**	**16**
d_m	Diameter of each microlens	96 μm	
D	Diameter of the aperture	7.55 mm	
N_s	Number of microlenses per row or column	60	
L_{om}	Distance between the flame centerline and mainlens	505 mm	
L_{mm}	Distance between the main lens and MLA	55.5 mm	
L_{mp}	Distance between the MLA and the photosensor	0.6 mm	
f	Focal length of the main lens	50 mm	
f_m	Focal length of the microlens	0.6 mm	

Case 1 **Case 2** **Case 3** **Case 4**

Single wavelength filter **Two wavelength filter array** **Three wavelength filter array** **Four wavelength filter array**

Fig. 5. Configuration of filter arrays design under different spectral bands.

3.2 Filter Array-based Multi-spectral LF Image

Fig. 6 shows the simulated multi-spectral LF flame images under different filter array designs in various MS-LFC configurations. For the single wavelength filter $\lambda_2 = 540$ nm (i.e., Case 1), only the pixel size and the number of pixels across the sub-image diameter vary, while all other camera parameters are kept constant. The flame contours in the simulated images remain consistent across different configurations. In the MS-LFC, the mainlens forms an intermediate image on the MLA plane, which is then resampled by the MLA to generate a series of sub-images. Since the incident ray passes through the filter array at the aperture, each sub-image retains the spectral characteristics defined by its corresponding filter element. As the number of spectral bands increases, the angular sampling per wavelength decreases due to the limited total angular resolution. With the increase in pixel size d_p from 3 μm×3 μm to 6 μm×6 μm, it's obvious that the angular sampling becomes sparse. Although the angular sampling becomes sparser with larger pixel sizes, the MS-LFC still keeps sampling diversity.

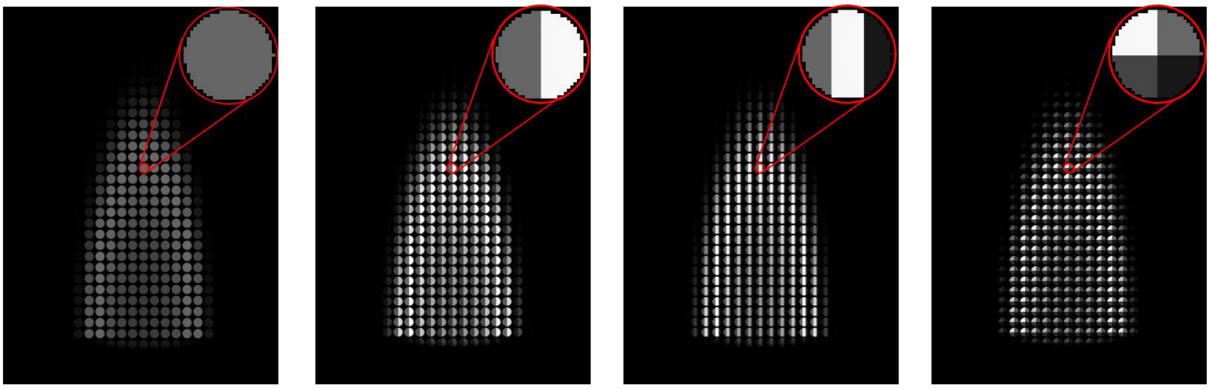

Case 1 **Case 2** **Case 3** **Case 4**

(a) Configuration 1

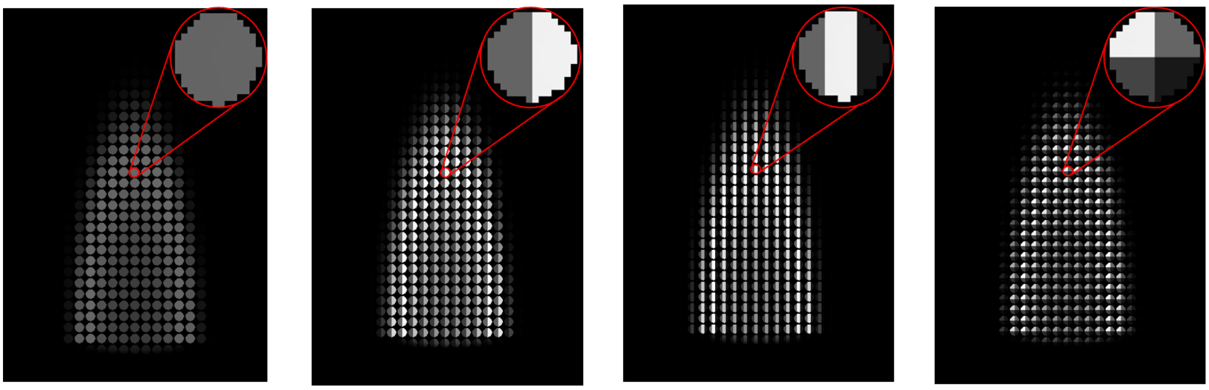

Case 1 **Case 2** **Case 3** **Case 4**

(b) Configuration 2

Fig. 6. Examples of simulated multi-spectral LF flame images under filter array designs and MS-LFC configurations.

The simulated multi-spectral LF image can be decoded by regrouping the pixels corresponding to the same angular direction (i.e., the same relative position behind the microlens). This process generates a set of sub-aperture images, each representing the flame as viewed from a distinct position within the main lens aperture. This effectively samples the LF from different viewpoints. Fig. 7 shows the generated sub-aperture images under different filter arrays and MS-LFC configurations. The spatial resolution of each sub-aperture image is determined by the number of microlenses in the array, as each image is formed by selecting one pixel from every microlens and rearranging these samples into a two-dimensional image. In this system, the microlens array contains 60 × 60 lenses, resulting in sub-aperture images with a resolution of 60 × 60 pixels. As the diameter of each microlens and the number of microlenses per row and column remain constant across different configurations, the resolution of the sub-aperture images also remains unchanged. However, the physical size of each sub-aperture image scales with the pixel size. Therefore, as the pixel size decreases, the physical size of each sub-aperture image becomes smaller. In addition, a reduction in the number of pixels along the diameter of each microlens leads to fewer available angular samples, resulting in a smaller number of generated sub-aperture images.

Furthermore, the spectral distribution of each sub-aperture image is consistent with that of the corresponding sub-image, leading to a spatial segmentation of the sub-aperture images into distinct regions, each associated with a different wavelength.

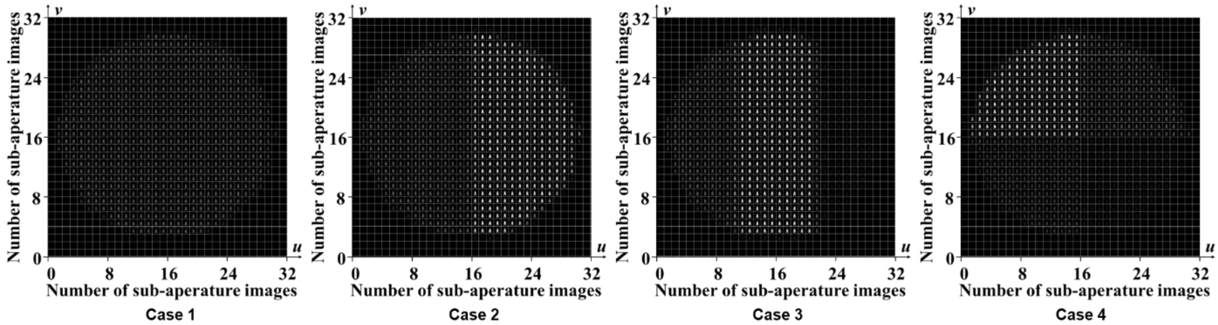

(a) Configuration 1

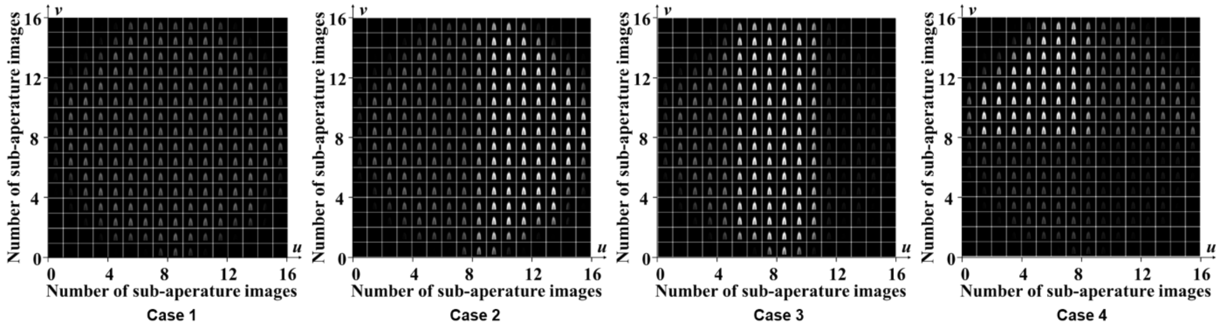

(b) Configuration 2

Fig. 7. Examples of sub-aperture images under different filter array designs and MS-LFC configurations.

3.3 Depth Resolution

Although the LF refocusing technique enables image generation at arbitrary depths, this does not imply that adjacent depth layers can be effectively distinguished due to limited depth resolution. Therefore, it is essential to investigate the depth resolution of the MS-LFCs. In the simplified 2D u-x space, known as the epipolar image plane, the LF projections of flame points at different depths appear as lines with depth-dependent slopes s. A point located at the focal depth F corresponds to a vertical line. Points deeper than F (i.e., farther from the camera) produce lines with positive s, while points closer than F result in lines with negative s.

In this study, in the epipolar image, s is utilized to analyze the depth resolution. The MS-LFC under Configuration 1 with a wavelength filter $\lambda_1 = 610$ nm is used for the analysis. The range of s is set from – 0.5 to 0.5, and three intervals Δs = 0.0100, 0.0125, and 0.0250 are investigated [19, 30]. For each interval, a stack of refocused images is generated using the method described in Section 2.2. The Tenengrad function is utilized to evaluate the sharpness of the refocused images quantitatively. To enable consistent comparison across different image stacks, the sharpness values are normalized by dividing each value by the maximum sharpness obtained within the corresponding stack. The normalized sharpness results for different Δs are presented in Fig. 8. The number of refocused images generated corresponds to Δs are (1) 101 images for an interval of 0.0100, (2) 81 images for 0.0125, and (3) 41 images for 0.0250. Although 101 refocused images can be generated at $\Delta s = 0.0100$, the refocused images corresponding to s values of -0.40 and -0.39 show a noticeable drop in sharpness, suggesting a failure to accurately resolve adjacent depth layers. At Δs = 0.0125 and 0.0250, the refocused image sharpness shows a similar variation, with maximum sharpness observed at the focal plane. Nevertheless, $\Delta s = 0.0125$ allows for a greater number of refocused images, thereby achieving higher depth resolution. Therefore, Δs = 0.0125 is selected for generating the stack of refocused images of the MS-LFC in the analysis, with each stack consisting of 81 refocused images.

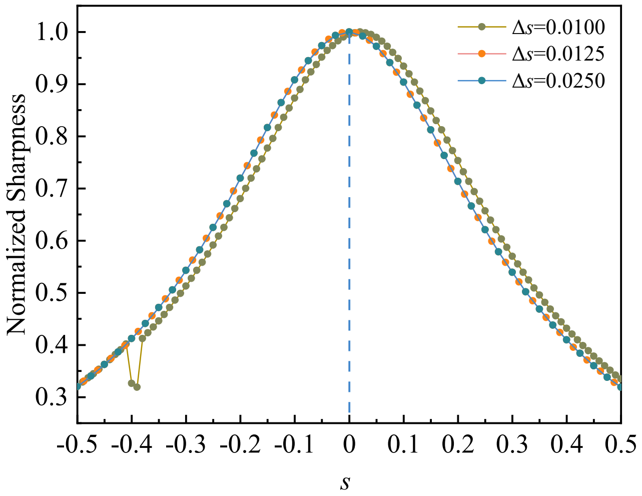

Fig. 8. Sharpness of the refocused image under different depth resolutions.

Fig. 9 presents the representative refocused images obtained with a wavelength filter $\lambda_1 = 610$ nm across multiple depths under different MS-LFC configurations. To enhance visual clarity, the intensity information in the images is displayed using the *hot* colormap. It can be observed that the refocused image appears sharpest at the focal plane and gradually becomes blurred as the refocusing depth moves away from it.

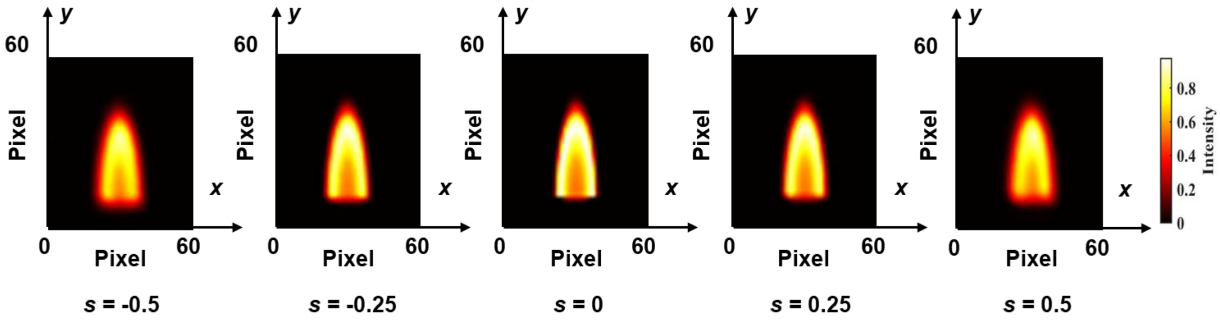

(a) Configuration 1

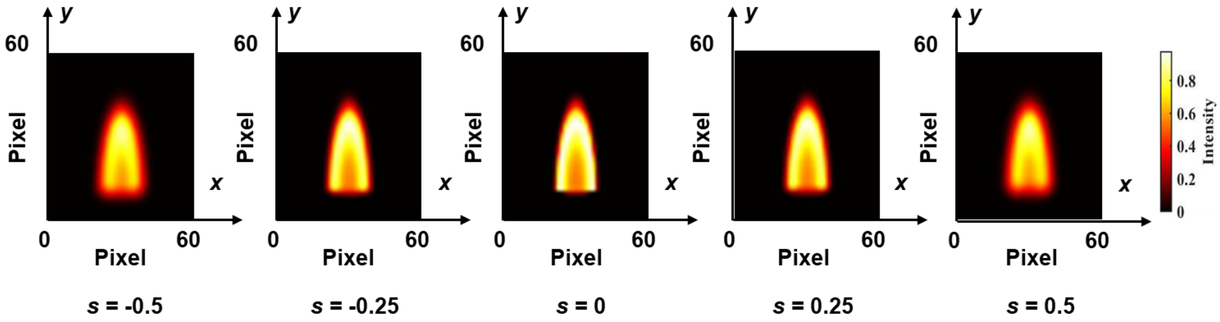

(b) Configuration 2

Fig. 9. Examples of the refocused images at different depths (Colormap is used for visualization purposes only).

3.4 Sharpness Assessment

To assess the sharpness of the refocused images obtained with the MS-LFC, refocused images at different depths under different MS-LFC configurations are analyzed. Fig. 10 presents the sharpness variation of the refocused images with λ_1 = 610 nm under different MS-LFC configurations. Table 2 summarizes the normalized sharpness values of the focal plane images. The variation in refocused image sharpness with depth shows a consistent trend across configurations, with increased sharpness observed as the refocused depth approaches the focal plane. However, the sharpness at the focal plane varies among different configurations, indicating that filter array design influences the sharpness of the refocused image.

For λ_1 = 610 nm under Configuration 1, Cases 1 and 3 (i.e., single-wavelength filter and three-wavelength filter array) show identical sharpness variation in the refocused image. Moreover, in Case 3, the sub-aperture images corresponding to λ_1 = 610 nm are centrally distributed, resulting in the same image sharpness as in Case 1. This is because the total number of sub-aperture images is large under Configuration 1, and the angular differences between neighboring sub-apertures are small. Therefore, even though only a subset of sub-apertures is used in Case 3, the selected views remain close in angle to those in Case 1, leading to similar refocusing sharpness variation.

A comparison of Cases 1, 2 and 4 (single wavelength filter, two wavelength filter array and four wavelength filter array) demonstrates that when the refocusing plane is distant from the focal plane, the refocused image becomes sharper with fewer sub-aperture images. Conversely, near the focal plane, image sharpness improves as the number of sub-aperture images increases. This is because the number of sub-aperture images affects the sampling density and phase correction in the frequency domain. When the refocusing plane is distant from the focal plane points in the scene, shift significantly, causing rapid phase changes that lead to aliasing and noise if a large number of sub-aperture images are used. Therefore, fewer sub-aperture images reduce aliasing and improve clarity. Conversely, near the focal plane, phase changes are small and more sub-aperture images provide higher sampling density, better preserving image details and improving sharpness. Furthermore, the sharpness of the focal plane image decreases as the number of sub-aperture images used during the refocusing process decreases from Cases 1 to 4, indicating that insufficient angular sampling adversely affects the sharpness of the refocused image at the focal plane.

As shown in Fig. 10 (b), for $\lambda_1 = 610$ nm under Configuration 2, the total number of sub-aperture images is only 1/4 of that in Configuration 1. This results in sparser angular sampling and larger angular differences between neighboring sub-apertures. Case 3 uses a subset of centrally distributed sub-aperture images, which produces the sharpest focal plane image among the cases. Furthermore, the comparison among Cases 1, 2, and 4 demonstrates that a reduction in the number of sub-aperture images used for refocusing leads to decreased image sharpness.

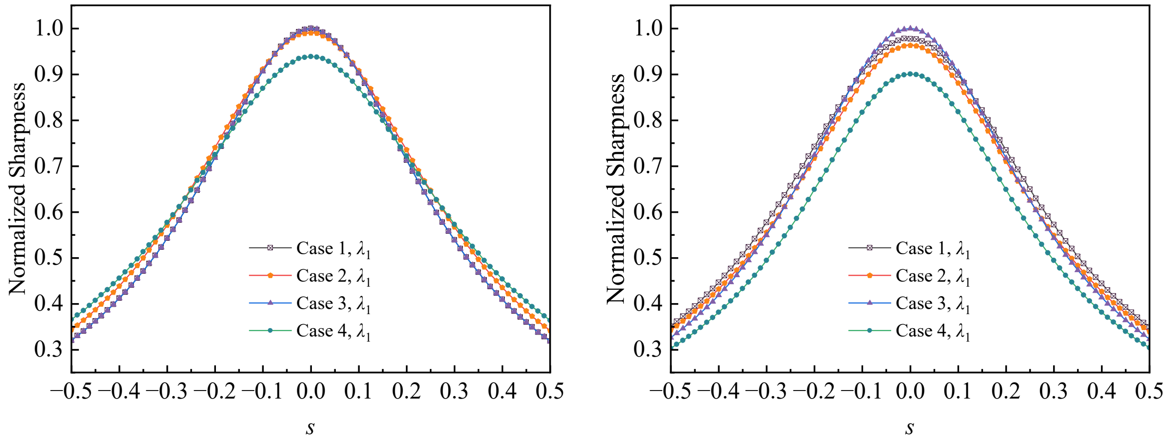

(a) Configuration 1

(b) Configuration 2

Fig. 10. Refocused image sharpness at $\lambda_1 = 610$ nm for various filter array designs and MS-LFC configurations.

Table 2. Overview of the normalized sharpness value of the focal plane image of $\lambda_1 = 610$ nm.

Cases	**Normalized Sharpness Value (a. u.)**	
	Configuration 1	**Configuration 2**
1	1.000	0.977
2	0.990	0.963
3	1.000	1.000
4	0.938	0.900

Fig. 11 shows the sharpness of the refocused images with $\lambda_2 = 540$ nm under different MS-LFC configurations, and the normalized sharpness values of the focal plane images can be seen in Table 3. A similar variation trend of refocused image sharpness is observed in the study of $\lambda_2 = 540$ nm under Configuration 1 of the MS-LFC. When the refocusing plane is far from the focal plane, fewer sub-aperture images used in the refocusing process result in sharper images. Conversely, near the focal plane, refocused image sharpness improves as the number of sub-aperture images increases. An exception is Case 3, where the refocused image sharpness near the focal plane is slightly lower than that of Case 4.

This is because, as shown in Fig. 5, the sub-aperture images of $\lambda_2 = 540$ nm in Case 3 are mainly distributed on the left side of the sub-aperture array, lacking central sub-aperture images, which leads to a slightly reduced sharpness near the focal plane. The sharpness values at the focal plane are 0.952 and 0.955 for Cases 3 and 4, respectively. For the study of $\lambda_2 = 540$ nm under Configuration 2 of the MS-LFC, as the total number of sub-aperture images decreases and the angular difference between sub-apertures increases, the sharpness of the refocused image decreases with fewer sub-aperture images used during refocusing, except for Case 3.

The above results demonstrate that with a large number of sub-aperture images and small angular differences between neighbouring sub-aperture images, using fewer sub-aperture images during refocusing can produce sharper images at planes far from the focal plane. Conversely, near the focal plane, increasing the number of sub-aperture images improves refocused image sharpness. When the number of sub-aperture images is small and the angular differences between neighbouring sub-apertures are large, using fewer sub-aperture images during refocusing decreases the sharpness of the refocused image. Furthermore, the sharpness of the refocused image is influenced by the spatial distribution of the selected sub-aperture images. Those distributed closer to the centre tend to produce clearer images at the focal plane.

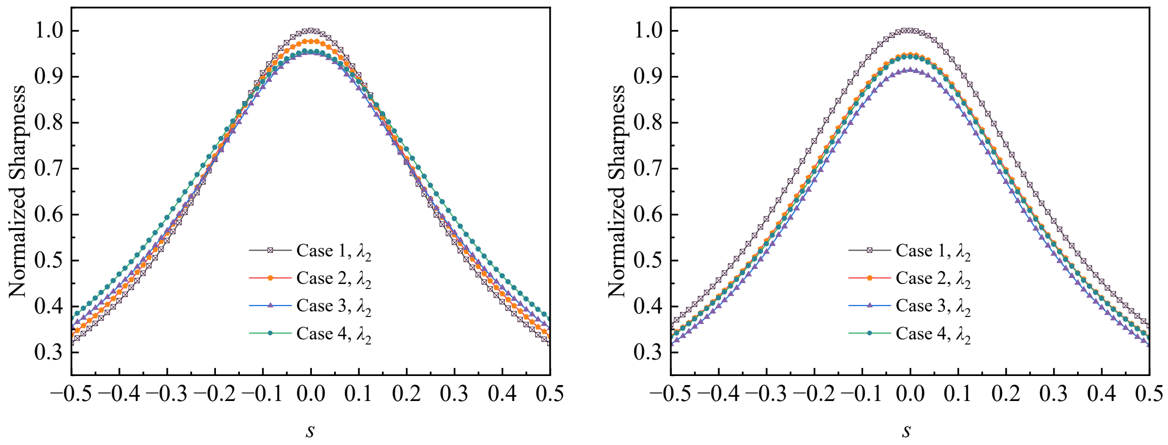

(a) Configuration 1

(b) Configuration 2

Fig. 11. Refocused image sharpness at $\lambda_2 = 540$ nm for various filter array designs and MS-LFC configurations.

Table 3. Overview of the normalized sharpness value of the focal plane image of $\lambda_2 = 540$ nm.

Cases	**Normalized Sharpness Value (a. u.)**	
	Configuration 1	**Configuration 2**
1	1.000	1.000
2	0.977	0.948
3	0.952	0.914
4	0.955	0.943

3.5 Similarity Assessment

To evaluate the similarity of refocused images obtained with the MS-LFC, refocused images at different spectra and depths under various MS-LFC configurations are analysed. The Structural Similarity Index

(SSIM) is calculated to quantitatively assess their similarity. For consistent comparison, the SSIM for each filter array design was obtained by comparing its refocused image with the corresponding single-wavelength reference image acquired under the same wavelength, depth and configuration.

Fig. 12 presents the SSIM of the refocused images at λ_1 = 610 nm under different MS-LFC configurations. In the study of λ_1 = 610 nm under Configuration 1, it can be observed that Case 2 and Case 3 (i.e., two-wavelength and three-wavelength filter arrays) exhibit the same structural similarity as Case 1 (i.e., single-wavelength filter). In contrast, Case 4 (i.e., four wavelength filter array) shows a noticeable decrease in SSIM, especially when the refocused depth is far from the focal plane. This is because only 1/4 of the sub-aperture images are used for refocusing, resulting in the loss of a significant amount of useful angular information. Nevertheless, the SSIM remains above 96% for Case 4. For λ_2 = 540 nm under Configuration 2, a similar trend can be observed. However, the SSIM between Case 4 and Case 1 is relatively high under this configuration. This is because, when refocusing is performed using only the top-left 1/4 of the sub-aperture images, the difference in similarity performance depends on the number of sub-apertures. When the sub-aperture resolution is low (e.g., Configuration 2), the angular sampling is sparse with limited redundancy. Therefore, using only a small part of the sub-aperture images is still sufficient to reconstruct a refocused image with SSIM close to that obtained using the full set. In contrast, when the sub-aperture resolution is high (e.g., Configuration 1), the angular sampling becomes denser and has richer angular information. In this case, removing 3/4 of the sub-aperture images causes a more severe loss of angular information, leading to a larger deviation from the full image refocusing result and a lower SSIM.

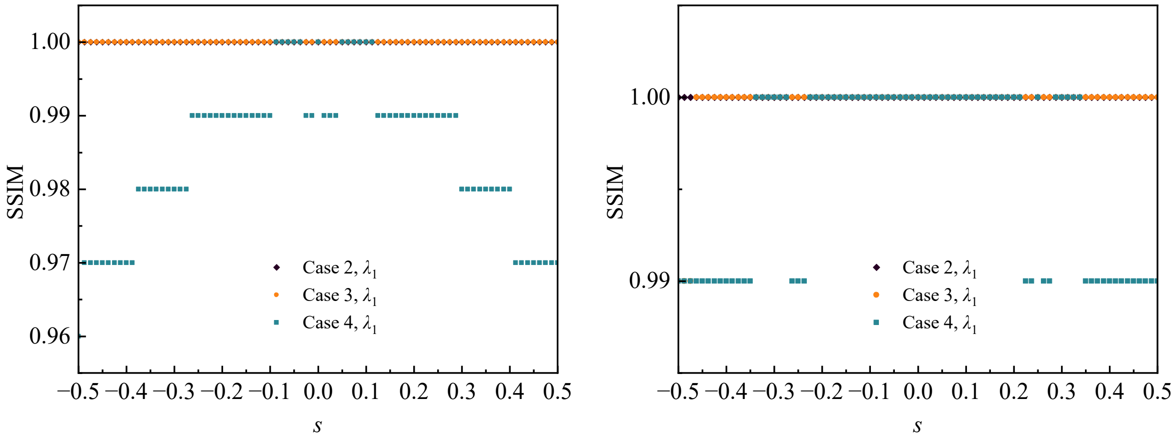

(a) Configuration 1

(b) Configuration 2

Fig. 12. Comparison of SSIM of refocused images at λ_1 = 610 nm, various filter array designs (Cases 2 to 4) and MS-LFC configurations.

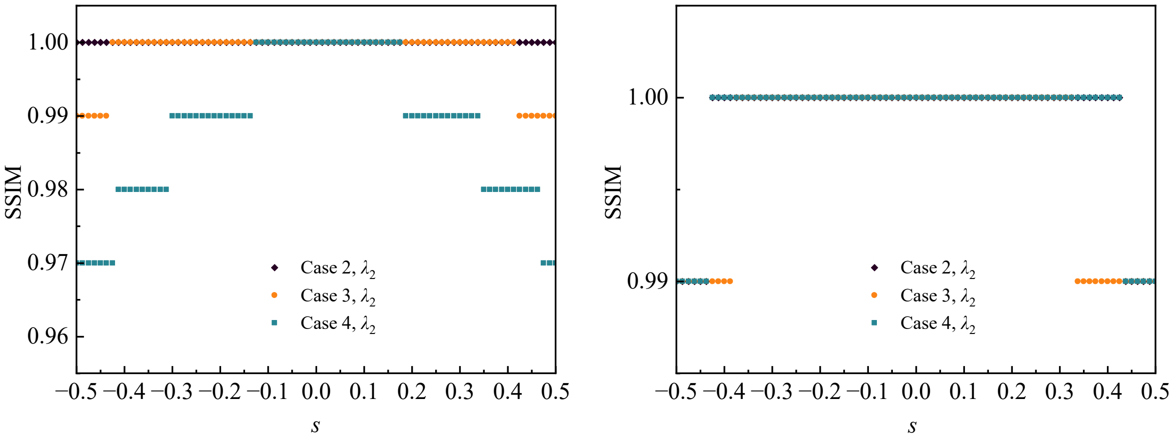

(a) Configuration 1 (b) Configuration 2

Fig. 13. Comparison of SSIM of refocused images at $\lambda_2 = 540$ nm, various filter array designs (Cases 2 to 4) and MS-LFC configurations.

The SSIM of the refocused images with $\lambda_2 = 540$ nm under different MS-LFC configurations is presented in Fig. 13. For $\lambda_2 = 540$ nm under Configuration 1, only Case 2 achieves the same SSIM as Case 1. For Case 3, since $\lambda_2 = 540$ nm occupies only the sub-aperture images on the left side, the available angular sampling is inherently limited. As a result, the SSIM decreases when the refocused depth is far from the focal plane. Case 4 exhibits a similar trend to that observed with $\lambda_1 = 610$ nm. Using only the top-right 1/4 of sub-aperture images causes a significant loss of angular information, especially when the total number of sub-apertures is large, resulting in lower structural similarity compared to the reference Case 1. For $\lambda_2 = 540$ nm under Configuration 2, it is observed that when the refocused depth is far from the focal plane, the SSIM between Case 2, Case 3, and Case 4 and the reference Case 1 remains at 0.99. As the refocused depth approaches the focal plane, the SSIM of all cases converges, ultimately reaching 1.

It can be concluded that the SSIM reveals that the similarity of refocused images is influenced by both the number and spatial distribution of sub-aperture images, as well as the spectral band and MS-LFC configurations.

3.6 Refocused Focal Plane Images

To evaluate the refocusing performance of the MS-LFC, refocused focal-plane images at different spectral bands are generated under various filter-array designs and MS-LFC configurations. Fig. 14 shows the refocused focal-plane images obtained with different MS-LFC configurations. To enhance visual clarity, image intensity is displayed using the *hot* colormap. Despite variations in filter-array design, the refocused focal-plane images for each spectral band are largely consistent. Furthermore, comparisons across MS-LFC configurations show similar consistency in the refocused images. These results demonstrate that the MS-LFC can simultaneously capture refocused images of flames at multiple wavelengths and depths.

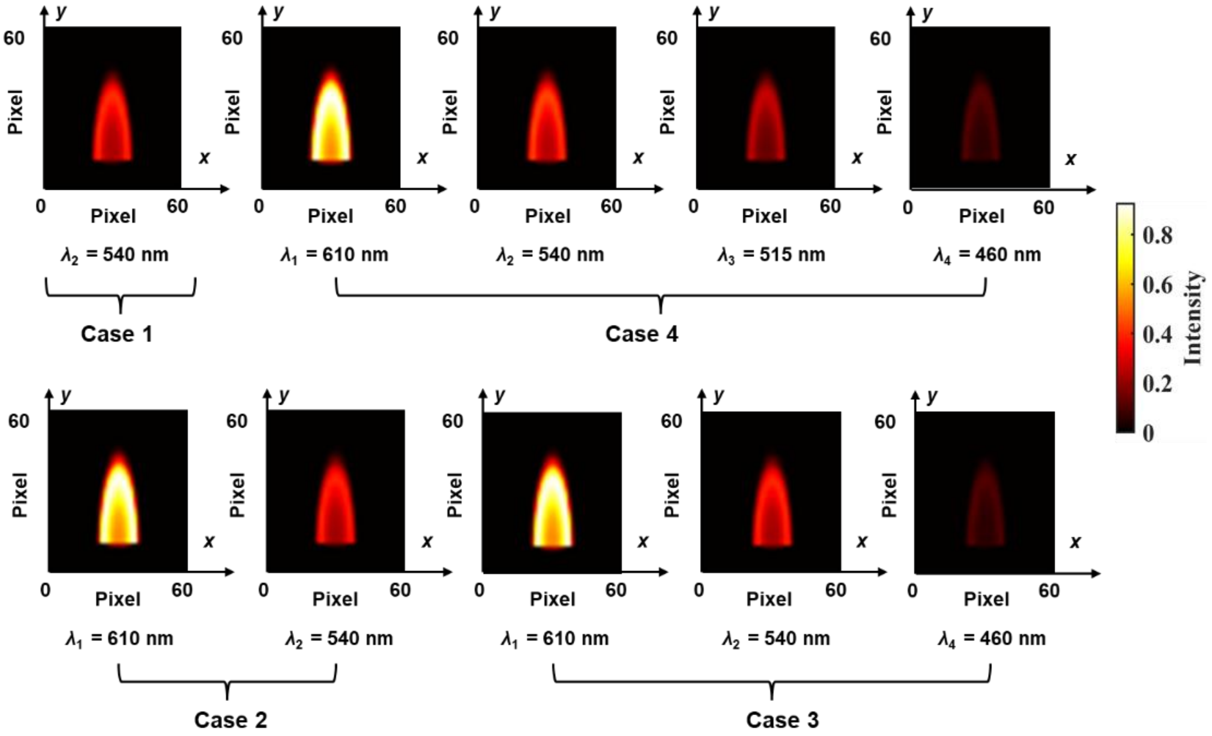

(a) Configuration 1

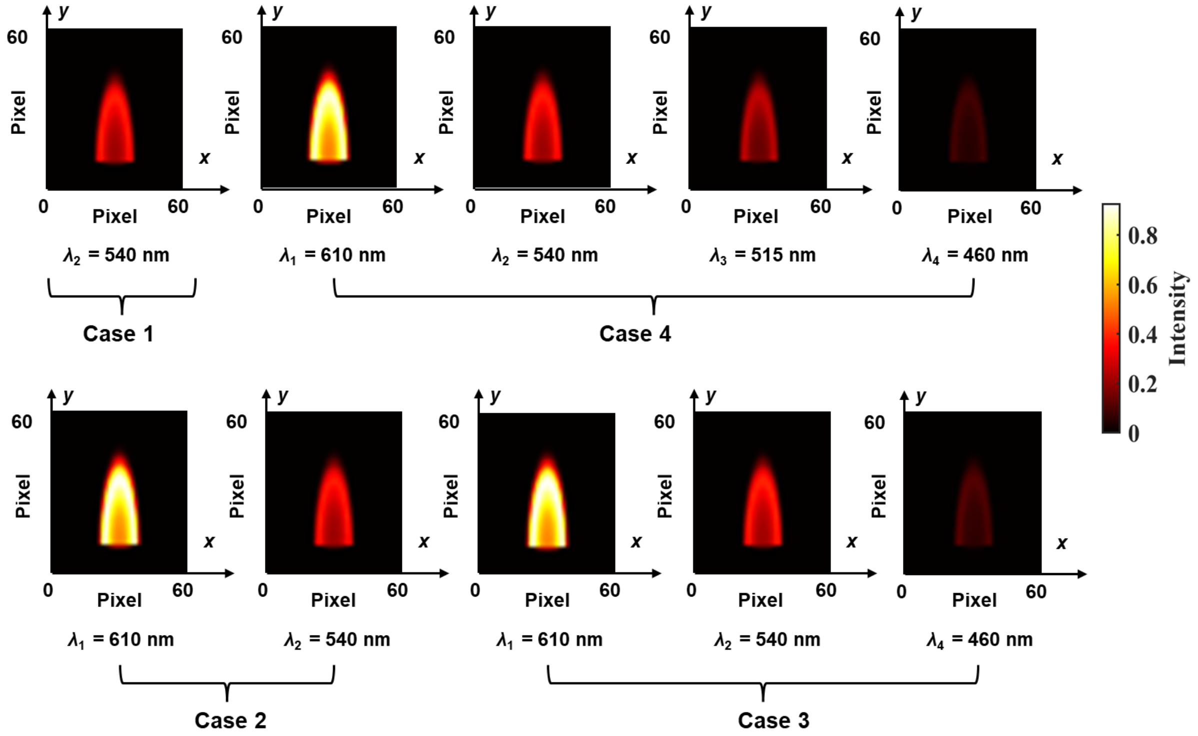

(b) Configuration 2

Fig. 14. Refocused focal plane images of different spectra under different MS-LFC configurations (Colormap is used for visualization purposes only).

4. Conclusions

This study systematically evaluates the impact of filter array designs and MS-LFC configurations on the quality of refocused flame images. Extensive simulations using sharpness and similarity metrics quantified their influence across different spectra and depths, providing a detailed assessment of the refocusing performance of the MS-LFC. These results offer theoretical insights and design guidelines for MS-LFC systems to enhance depth-resolved combustion diagnostics. The main conclusions and design recommendations for the MS-LFC are summarised as follows:

- The results demonstrate that filter array design and MS-LFC configurations are decisive in determining refocused image quality. Centrally distributed wavelengths and angular samples consistently yield superior in-focus sharpness. Angular sparsity, when properly structured, can preserve refocusing quality under certain depth conditions.

- In addition, although aggressive reduction in the number of sub-aperture images leads to degraded overall similarity, maintaining sufficient angular coverage effectively preserves focal-plane fidelity. These findings establish fundamental design principles for balancing resolution trade-offs in MS-LFC systems.

- Based on the analysis, several practical guidelines for the design of the MS-LFC system are derived. These include prioritising centrally concentrated spectral distributions, optimised angular sampling strategies and appropriate sub-aperture choice under constrained acquisition conditions. Collectively, these guidelines provide actionable insight for improving the robustness, efficiency and imaging quality of depth-resolved multispectral flame diagnostics.

As the proposed system has not been validated using real experimental data, experimental validation is crucial for demonstrating its practical applicability. Future work will focus on experimental validation using a MS-LFC prototype system and extending the framework to real-time multi-spectral 3D flame reconstruction.

Acknowledgement

The authors wish to express their gratitude to the Engineering & Physical Sciences Research Council (EPSRC) Project Reference: EP/X020789/1.

References

1. Wang, Z., J. Dai, and S. Yang, The development of a multispectral pyrometer for achievable true temperature field measurements of the explosion flame. Measurement Science and Technology, 2023. **34**(6).
2. An, Q., et al., Flame stabilization mechanisms and shape transitions in a 3D printed, hydrogen enriched, methane/air low-swirl burner. International Journal of Hydrogen Energy, 2021. **46**(27): p. 14764-14779.
3. Bouvier, M., et al., On the use of PIV, LII, PAH-PLIF and OH-PLIF for the study of soot formation and flame structure in a swirl stratified premixed ethylene/air flame. Proceedings of the Combustion Institute, 2021. **38**(1): p. 1851-1858.

4. Krabicka, J., G. Lu, and Y. Yan, Profiling and Characterization of Flame Radicals by Combining Spectroscopic Imaging and Neural Network Techniques. IEEE Transactions on Instrumentation and Measurement, 2011. **60**(5): p. 1854-1860.

5. Yao, C., et al., Multi-spectral light-field imager for ultra-high temperature measurement. Opt Express, 2024. **32**(18): p. 32094-32106.

6. Fernandez, S.F., et al., Soot and spectral radiation modeling for high-pressure turbulent spray flames. Combustion and Flame, 2018. **190**: p. 402-415.

7. Brisley, P.M., et al., Three-dimensional temperature measurement of combustion flames using a single monochromatic CCD camera. IEEE Transactions on Instrumentation and Measurement, 2005. **54**(4): p. 1417-1421.

8. Sun, J., et al., Three-dimensional temperature field measurement of flame using a single light field camera. Opt Express, 2016. **24**(2): p. 1118-32.

9. Khan, A., et al., Realistic Object Reconstruction Under Different Depths Through Light Field Imaging for Virtual Reality. IET Image Processing, 2025. **19**(1).

10. Ng, R., Digital light field photography. 2006, Stanford University.

11. Georgeiv, T. and C. Intwala, Light Field Camera Design for Integral View Photography. 2008.

12. Zhao W, Zhang B, and X. C, Optical Sectioning Tomographic Reconstruction of Three-dimensional Flame Temperature Distribution Using Single Light Field Camera. IEEE Sensors Journal, 2018. **18**(3): p. 528-539.

13. Liu, Y., et al., Spatial resolution of light field sectioning pyrometry for flame temperature measurement. Optics and Lasers in Engineering, 2021. **140**: p. 106545.

14. Zhang, B., et al., Reconstruction of 3D Temperature Profile of Radiative Participatory Flame Based on Digital Refocusing Technique of Light Field Camera. International Journal of Photoenergy, 2019. **2019**: p. 1-13.

15. Jin, Y., et al., Three-dimensional dynamic measurements of CH* and C2* concentrations in flame using simultaneous chemiluminescence tomography. Opt Express, 2017. **25**(5): p. 4640-4654.

16. Levoy, M., et al., Light field microscopy. ACM Trans. Graph., 2006. **25**(3): p. 924–934.

17. Horstmeyer, R., R. Athale, and G. Euliss, Modified light field architecture for reconfigurable multimode imaging. SPIE Optical Engineering + Applications. Vol. 7468. 2009: SPIE.

18. Fahringer, T.W., et al., Design of a multispectral plenoptic camera and its application for pyrometry. Appl Opt, 2022. **61**(10): p. 2459-2472.

19. Huang, Y., et al., Data rectification and decoding of a microlens array-based multi-spectral light field imaging system. Optics and Lasers in Engineering, 2024. **180**.

20. Luan, Y., D. Mei, and S. Shi, Light-field multi-spectral radiation thermometry. Opt Lett, 2021. **46**(1): p. 9-12.

21. Kelly, D.L., D.E. Scarborough, and B.S. Thurow, A novel multi-band plenoptic pyrometer for high-temperature applications. Measurement Science and Technology, 2021. **32**(10).

22. Kelly, D., et al., Simultaneous tomographic multi-component reconstructions using multispectral plenoptic cameras, in Applied Optical Metrology V. 2023.

23. Levoy, M. and P. Hanrahan. Light field rendering. in Proceedings of the 23rd annual conference on Computer graphics and interactive techniques. 1996. ACM.

24. Dansereau, D.G., O. Pizarro, and S.B. Williams, Linear Volumetric Focus for Light Field Cameras. ACM Trans. Graph., 2015. **34**(2): p. Article 15.

25. Lu, X., C. Li, and T. Liu, Research on the Evaluation Method of Reference free Clarity for Aerospace Optical Images, in 2024 IEEE 4th International Conference on Information Technology, Big Data and Artificial Intelligence (ICIBA). 2024. p. 442-446.

26. Hore, A. and D. Ziou, Image Quality Metrics: PSNR vs. SSIM, in 2010 20th International Conference on Pattern Recognition. 2010. p. 2366-2369.

27. Qi, Q., et al., Approach to reduce light field sampling redundancy for flame temperature reconstruction. Optics Express, 2021. **29**(9): p. 13094-13114.

28. Liu, Y., et al., Investigation and optimization of sampling characteristics of light field camera for flame temperature measurement. Chinese Physics B, 2019. **28**(3): p. 034207.

29. Sun, J., et al., Investigation of flame radiation sampling and temperature measurement through light field camera. International Journal of Heat and Mass Transfer, 2018. **121**: p. 1281-1296.

30. Ng, R., Digital light field photography. 2006: Stanford University.